

Event-Driven Encoding Algorithms for Synchronous Front-End Sensors in Robotic Platforms

*Original*

Event-Driven Encoding Algorithms for Synchronous Front-End Sensors in Robotic Platforms / Ros, P. M.; Laterza, M.; Demarchi, D.; Martina, M.; Bartolozzi, C.. - In: IEEE SENSORS JOURNAL. - ISSN 1530-437X. - ELETTRONICO. - 19:16(2019), pp. 7149-7161. [10.1109/JSEN.2019.2911668]

*Availability:*

This version is available at: 11583/2755952 since: 2021-11-08T17:01:32Z

*Publisher:*

Institute of Electrical and Electronics Engineers Inc.

*Published*

DOI:10.1109/JSEN.2019.2911668

*Terms of use:*

This article is made available under terms and conditions as specified in the corresponding bibliographic description in the repository

*Publisher copyright*

IEEE postprint/Author's Accepted Manuscript

©2019 IEEE. Personal use of this material is permitted. Permission from IEEE must be obtained for all other uses, in any current or future media, including reprinting/republishing this material for advertising or promotional purposes, creating new collecting works, for resale or lists, or reuse of any copyrighted component of this work in other works.

(Article begins on next page)

# Event-Driven Encoding Algorithms for Synchronous Front-End Sensors in Robotic Platforms

Paolo Motto Ros<sup>2\*</sup>, *Member, IEEE*, Marino Laterza<sup>1\*</sup>, Danilo Demarchi<sup>3</sup>, *Senior Member, IEEE*,  
Maurizio Martina<sup>3</sup>, *Senior Member, IEEE*, and Chiara Bartolozzi<sup>1</sup>, *Member, IEEE*

**Abstract**—Asynchronous, event-driven, sampling techniques adapt the sampling rate of sensory signals to their dynamics, by effectively compressing the data with respect to synchronous, clock-driven, sampling. In robotics such techniques offer data and bandwidth reduction, together with high temporal resolution and low latency. Despite vision and auditory event-driven sensors are currently available, robots are still equipped with a plethora of other sensors that might benefit from the event-driven encoding. In this paper, we study five estimation algorithms that implement event-driven encoding for off-the-shelf clock-driven sensors. Digital accelerometer datasets were used to validate the system in robotic applications; other datasets have been used to assess the general performance of the proposed approach. The two best algorithms in terms of six performance parameters have been implemented on a Xilinx Artix-7 FPGA platform, using 2892 LUTs and 3620 flip-flops and reducing the output bandwidth from -44 % to -75 %, over the considered datasets.

**Index Terms**—Asynchronous sampling algorithms, Event-Driven, FPGA, Relative Threshold, Output Bandwidth, Robotic Environment.

## I. INTRODUCTION

State-of-the-art sensors are mostly based on clock-driven sampling of the physical signal being measured. This approach has a trade-off between the amount of data acquired and the maximum detectable input frequency (Nyquist) of the signal variation. Tuning the clock-rate for very fast signals results in sampling redundant values when the signal is slowly changing, while decreasing the sampling frequency results in missing potentially important signal variations. Additionally, for sensors with multiple sensing sites, such as cameras or large area tactile devices, there is an inherent latency in data transmission, due to the need to synchronously sample all the sensing elements in the device. While the advantage of clock-driven sampling is the compliance of all sensors and acquisition devices to the clock-driven paradigm, the trade-offs and downsides listed above are detrimental for building efficient sensory systems for artificial devices. Specifically, data compression, high temporal resolution and short latency are

especially desirable in robotics, where the progressive application in unconstrained scenarios is leading to the integration of an increasing number of sensors needed to perceive both the environment and the status of the robot. A viable alternative is the “neuromorphic” event-driven sensing strategy inspired by biological sensory systems, where the sensing element (e.g. photoreceptors and retinal cells in vision, mechanoreceptors in touch) gets active when it detects a variation in its own input and sends action potentials to neurons in the sensing areas of the brain. The output activity of each sensing neuron encodes for the properties of the sensed stimulus. Similar approaches (eventually sending a sample along with the event) have been investigated and developed in other research areas too, including (but not limited to) automation control and signal processing [4] and energy metering [5].

Neuromorphic event-driven sensing sends data only when the amplitude of the measured signal has experimented a certain change, rather than at fixed time intervals. This change could be referred to the sample which generated the last event [1]. The signal is assumed to stay constant until another event is produced. As a consequence, the reference value could be exploited as a predictor for the future values of the signal. If this estimate differs from the actual sample value by more than a given amount, then a new event is generated. In this encoding scheme, the data is written on the output bus as soon as the change is sensed. In a scenario with many sensing sites (e.g., vision or tactile), this strategy decreases latency dramatically, avoiding the sampling and transmission of the whole set of pixels (or taxels). Information is then encoded in the relative timing between generated events and the value of the sample is not sent, limiting the number of bits to be sent, as opposed to other asynchronous sampling transmissions, which send the whole data sample whenever a threshold-crossing occurs [2]–[4].

This approach resulted so far in the design of event-driven vision [8]–[10], [12], auditory [11] and (more recently) tactile sensing [13], [18], [22], where the sensing element itself implements the data-driven sampling. While event-driven vision sensors have already been integrated on robotic platforms, tactile sensors require further development [21] and other sensor modalities are not yet under development. On the other hand, robots are fully equipped with a plethora of sensors (temperature, pressure, encoders, accelerometers, etc.) and it is possible to emulate event-driven compression using traditional off-the-shelf clock-driven sensors that are readily integrated in robotic environments. The aim of this approach is two-fold: improving efficiency in signal transmission (optimizing

\* M. Laterza and P. Motto Ros equally contributed to this manuscript

<sup>1</sup> M. Laterza and C. Bartolozzi are with iCub Facility, Istituto Italiano di Tecnologia, Genova, Italy, E-mail: marino.laterza@iit.it, chiara.bartolozzi@iit.it

<sup>2</sup> P. Motto Ros is with Electronic Design Lab, Istituto Italiano di Tecnologia, Genova, Italy, E-mail: paolo.mottoros@iit.it

<sup>3</sup> M. Martina and D. Demarchi are with Dipartimento di Elettronica e Telecomunicazioni, Politecnico di Torino, Torino, Italy, E-mail: maurizio.martina@polito.it, danilo.demarchi@polito.it

bandwidth, data compression, latency, etc.) and delivering prototype systems for the development of event-driven algorithms for perception. An example of emulation of event-driven sensing of clock-based data has been shown in [20], where the event-driven data encoding and transmission have been implemented on an FPGA interfaced to the capacitive sensors of the iCub robot skin [24]. Other applications have been developed in the prosthetic field [14], with the aim of implementing a tactile feedback control, based on the actual data sensed by the prosthesis.

Algorithms proposed for the conversion of clock-sampled data into event-driven show the potential compression performance of this approach. They are based on detection of relative change among current and previous samples. Specifically, the detected change is relative to the absolute value ( $\Delta x/x$ ), de facto implementing a logarithmic compression that increases the compression dynamic range.

In this work, we characterize a set of more complex algorithms, analyzing their performance in terms of data compression and implementation cost. Our goal is to find an algorithm for event-driven encoding that can be applied to any sensory signal acquired by a clock-sampling strategy.

As case study, we tested the algorithms for the encoding of MEMS accelerometers that are integrated in the iCub humanoid robotic platform [24]. As discussed in [20], the mid-term goal is to have a unified tactile/accelerometric sensing system in order to enable the development of event-driven applications — allowing the humanoid robot to interact with the surrounding environment — without requiring the development of new sensors. With this aim, one of the requirements has been to use the same hardware platform (and to respect the same implementation constraints) as done in [20].

The conceived scheme is absolutely general and flexible, so that changing its internal parameters will produce good performance for very different sensors. To offer a thorough analysis of the encoding scheme, we frame it as an estimation problem and compare different solutions.

Starting from the asynchronous algorithm called “Send-on-Delta” [1], where the sample is transmitted when the absolute value of the difference between the current input and the previous one is greater than a given threshold, we also evaluated more complex algorithms. Those algorithms compare the input data with a reference value, in order to decide if an event has to be generated or not. As such, the reference value could be thought of as a predictor of the value of the next sample. For example, in the Send-on-Delta case, the predictor is a zero-order one. As a result, in this alternative view, if the estimation error falls within a given boundary with respect to the measured input, no event (and hence no transmission) is generated. Differently from the standard Send-on-Delta, in the proposed implementation, as soon as the estimation error exceeds the boundary, an event is generated and transmitted. The information is encoded in the exact time at which the event is generated and implicitly transmitted in the timing between events, hence, we do not need to send the absolute value of the sample together with the event. In order to bound the maximum relative error, the change with respect to the predicted sample value is computed using a relative

threshold.

The best-performing algorithms are then evaluated in terms of accuracy, output data rate reduction and resource requirement on a Xilinx Artix-7 FPGA (model XC7A35T-L1). Specifically, the accuracy parameter (the error between the original and the reconstructed signal) is used to check if and how much the proposed encoding reduces the information content of the signal, however, in neuromorphic perception the signal is not usually reconstructed and information about the sensed signal is extracted using event-driven algorithms. Also, the compression rate is used to compare the different proposed algorithms, rather than to find the best possible compression strategy for the signal at hand. For this reason, we treated agnostically the signal that we were processing, without using knowledge about the physical origin of the signal itself. That strategy could benefit a specific application, for example by considering the non-independence among the three axis of the accelerometers and the relationship between the position, velocity and acceleration values. In such a case, the compression would be higher, but specific to the accelerometer signal only. Rather, we were looking for a more general algorithm for the event-driven encoding of any sensory signal. In the accelerometer case, the architecture consists in three identical submodules, one per spatial axis, which implement the encoding scheme in parallel. The approach used to send the data on the bus is the so-called Address Event Representation (AER) [15]–[17], where the output data only includes the event polarity (e.g., if the signal is increasing or decreasing with respect to the previous sample) along with the corresponding address of the sensor (in this specific case, of the accelerometer axis). Consequently, the output bus exhibits an asynchronous flow of messages containing the sender address and some bits representing the event polarity information, instead of the whole sample value. As specific AER protocol, we use an implementation of the asynchronous serial AER [15]–[17], that is specifically designed for robotic systems, where minimizing wiring is a strict requirement. We first outline the main differences between the traditional asynchronous sampling schemes and the proposed one (Section II). After setting up the main features of the implemented scheme, the possible event polarities are discussed (Section III). Once the communication system is set, we make a comparison aimed at identifying the best predicting algorithm to embed inside the defined scheme (Section IV). Then, we evaluate the quantitative results of this analysis by means of several performance figures (Section V) and we implement the best-performing algorithms, as well as the communication system, on FPGA (Section VI). The main achievements of the work and future development are finally discussed (Section VII).

## II. EVENT-GENERATION SCHEME

### A. Pre-Algorithmic Manipulation of Data

The sampling rate of most commercial digital accelerometers ranges from units to thousands of Hz. It is suitable for a clock-based acquisition from this category of sensors, but an event-driven transmission requires a higher temporal precision. Specifically, the information in event-driven transmission is

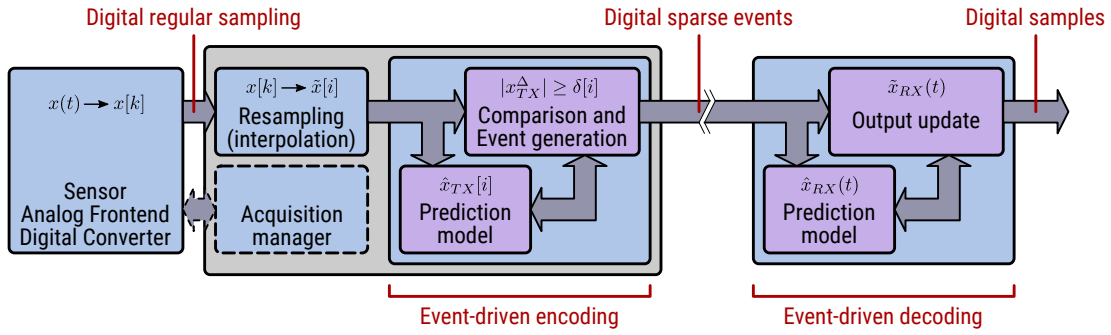


Fig. 1: Overall scheme of the proposed system: the analog signal  $x_{TX}(t)$  is first acquired by the sensor and then resampled at a higher  $1/T_s$  rate to improve the timing accuracy; by comparing the state variable  $x_{TX}^*$  with the interpolated  $x_{TX}^i$ , events are eventually generated (EvGen); on the decoding side, a corresponding state variable  $x_{RX}^*$  is combined with the reception of events in order to update the output variable  $x_{RX}''$ .

201 triggered exactly by change detection, whereas in clock-based  
 202 sampling this situation can happen between two consecutive  
 203 samples.

204 In the proposed implementation, we internally resample,  
 205 with a constant period  $T_s$ , the data received from the trans-  
 206 ducer  $x[k]$  that corresponds to  $x(kT)$  (in the discrete time  
 207 domain, regularly sampled with a period  $T$ ) using a linear in-  
 208 terpolator and resulting in  $\tilde{x}[i]$  that corresponds to  $\tilde{x}(iT_s)$  (with  
 209 the only constraint  $\tilde{x}(kT) = x(kT)$ , and, usually,  $T_s \ll T$ ).  
 210 The resampling rate has been fixed at 5 MHz, as in [20],  
 211 leading to a flow of produced samples every 200 ns. The denser  
 212 input mimics an analog continuous signal and allows to timely  
 213 detect the variation of the input signal, therefore increasing  
 214 the timing precision of the overall acquisition system. The  
 215 increased timing precision allows for a better reconstruction  
 216 of the signal, limiting the loss of information that would oc-  
 217 cur without signal interpolation. The corresponding hardware  
 218 block will contain a resampling unit, or resampler, feeding the  
 219 block implementing the event generation (EG).

### 220 B. Algorithm Scheme

221 Figure 1 shows the overall scheme of an event transmitter  
 222 (TX), including the event generation, and the receiver (RX),  
 223 including the sample reconstruction. The event generation  
 224 block computes the estimate for the sample at the next time  
 225 step — by using one of the algorithms detailed in Section III  
 226 — and compares it to the sample produced by the resampler.  
 227 When the absolute value of their difference exceeds a given  
 228 threshold, an event is generated. Namely, for each point of  
 229 the linear interpolation, a predicted value is computed: the  
 230 estimation always depends on the type of the last sent event  
 231 and it may further depend either on the last value(s) which  
 232 produced event(s) or on the last estimate(s).

233 In time-continuous asynchronous sampling algorithms [1]–  
 234 [4], [6], sampling (and therefore event generation, EvGen)  
 235 occurs whenever the absolute difference between the predicted  
 236 value and the input signal (sample) crosses a given (static)  
 237 threshold, i.e., we can define the sequence  $\mathcal{T} \triangleq \{t_i\}$  (with  
 238  $t_i \in \mathbb{R}^+$  and  $i \in \mathbb{N}$ ) as:

$$\mathcal{T} \triangleq \{t_i \mid |x_{TX}^\Delta(t_i)| \geq \delta(t_i) \wedge |x_{TX}^\Delta(t_i^-)| < \delta(t_i^-)\} \quad (1)$$

where  $\wedge$  refers to the logical AND operation, and we define

$$\begin{aligned} x_{TX}^\Delta(t) &\triangleq x_{TX}(t) - \hat{x}_{TX}(t) \\ \delta(t) &\triangleq \delta^* \end{aligned} \quad (2)$$

239 with  $\hat{x}_{TX}(t)$  the predicted value at  $t$ ,  $\delta(t)$  the threshold  
 240 set to a fixed value  $\delta^*$ . Since we are dealing with sample-  
 241 based sensors, with the output data eventually re-sampled or  
 242 interpolated (at a fixed rate, as described in Sec. II-A), we can  
 243 define a new sequence  $\mathcal{I} \triangleq \{i\}$ , corresponding to the sequence  
 244  $\{t_i = iT_s\}$  (with  $i \in \mathbb{N}$ ) of discrete time-points at which an  
 245 event is generated, as follows:

$$\mathcal{I} \triangleq \{i \mid |x_{TX}^\Delta[i]| \geq \delta[i] \wedge |x_{TX}^\Delta[i-1]| < \delta[i-1]\} \quad (3)$$

where we define

$$\begin{aligned} x_{TX}^\Delta[i] &\triangleq \tilde{x}_{TX}[i] - \hat{x}_{TX}[i] \\ \delta[i] &\triangleq \delta^* \end{aligned} \quad (4)$$

246 being  $\tilde{x}_{TX}[i]$  and  $\hat{x}_{TX}[i]$  the interpolated and predicted, re-  
 247 spectively, signals,  $\delta[i]$  the threshold set to a fixed (positive)  
 248 value  $\delta^*$ .

249 With this scheme, two events are sufficient to implement  
 250 an unambiguous communication. We can define a sequence  
 251 of events  $\mathcal{E} \triangleq \{E_i\}$ , with each  $E_i$  triggered at time  $t_i \in \mathcal{T}$  (in  
 252 case of time-continuous system) or, with the resampling (as  
 253 in this case), at  $i \in \mathcal{I}$ , as:

$$E_i = \begin{cases} E_\uparrow & \text{if } x_{TX}^\Delta[i] \geq \delta[i] \\ E_\downarrow & \text{if } x_{TX}^\Delta[i] \leq -\delta[i]. \end{cases} \quad (5)$$

254  $E_\uparrow$  and  $E_\downarrow$  are usually encoded by a polarity bit added to the  
 255 address of the event [8], [16], [17]. Events are transmitted from  
 256 the TX to the RX in real-time with a low-latency/low-overhead  
 257 point-to-point asynchronous AER protocol [19], [20], so that  
 258 events can be immediately processed by the RX.

259 On the RX side, whenever an event is received at time  
 260  $t$  (EvRcv( $t$ )), the corresponding  $\tilde{x}_{RX}(t)$  can be updated as  
 261 follows:

$$\tilde{x}_{RX}(t) = \begin{cases} \hat{x}_{RX}(t^-) + \delta(t) & \text{if EvRcv}(t) = E_\uparrow \\ \hat{x}_{RX}(t^-) - \delta(t) & \text{if EvRcv}(t) = E_\downarrow \\ \hat{x}_{RX}(t^-) & \text{otherwise} \end{cases} \quad (6)$$

where  $\hat{x}_{RX}(t)$  is the predicted value at time  $t$  by the RX.

This scheme, even if based simply on a difference, is not optimal in the application under investigation. Indeed, the accelerations provided by the sensor could go as high as 4 G and as low as -4 G, crossing the zero level, as proved in several datasets acquired on the iCub robotic equipment [24]. For an equal relative change (eg. 10% of the reference value), a fixed threshold produces more events for a higher sensor value. However, using fixed thresholds the sensitivity of the event generator is constant for the whole range of the sensor. The advantage of a relative threshold is that the produced number of events is constant for equal relative changes, but the sensitivity decreases for higher sensor values.

In order to obtain an homogeneous event rate over the whole range and to compare several algorithms for equal maximum relative error, a relative-threshold-based scheme has been used, instead. A fixed relative threshold is equivalent to a dynamic absolute one, so in the mathematical model described by equations (3) and (4) we can replace equation (4) with:

$$\delta[i] \triangleq \mu \cdot |\tilde{x}_{TX}[i]| \quad (7)$$

where  $\mu$  is the relative threshold, in the range (0, 1), and is a constant time-invariant tuning parameter, which is set once. As a consequence, the relative threshold  $\mu$  describes how the sensitivity of the event generator increases for small sensor values and how the sensitivity decreases for high sensor values. By substituting equation 7 in 3 we can rewrite 3 as:

$$\mathcal{I} \triangleq \{i \mid |x_{TX}^\delta[i]| \geq \mu \wedge |x_{TX}^\delta[i-1]| < \mu\} \quad (8)$$

where we define

$$x_{TX}^\delta[i] \triangleq \frac{\tilde{x}_{TX}[i] - \hat{x}_{TX}[i]}{\tilde{x}_{TX}[i]} \quad (9)$$

so to highlight the relative behavior (w.r.t.  $\tilde{x}_{TX}[i]$ ) of the event generation.

To summarize, an  $E_\uparrow$  event with a relative threshold  $\mu$  means that the interpolated value is, in absolute value,  $100\mu\%$  (or more) higher than the predicted one, whereas an  $E_\downarrow$  event means that the absolute value of the interpolated sample is  $100\mu\%$  (or more) lower than the corresponding predicted one. However, thanks to the resampling mechanism, an exact  $100\mu\%$  difference can be expected. This shall be confirmed by the software simulations on the considered input datasets, which are discussed in Section V.

As a result, the reconstructed signal at the receiver  $\tilde{x}_{RX}(t)$  can be obtained as follows:

$$\tilde{x}_{RX}(t) = \begin{cases} \hat{x}_{RX}(t^-) \cdot (1 + \mu) & \text{if EvRcv}(t) = E_\uparrow \\ \hat{x}_{RX}(t^-) \cdot (1 - \mu) & \text{if EvRcv}(t) = E_\downarrow \\ \hat{x}_{RX}(t^-) & \text{otherwise} \end{cases} \quad (10)$$

where  $\hat{x}_{RX}(t)$  is the predicted value at time  $t$  by the RX.

Here, when no event is received, the predicted value  $\hat{x}_{RX}(iT_s)$  is within  $\tilde{x}_{TX}(iT_s) \cdot (1 \pm \mu)$ .

As  $(1 + \mu)$  and  $(1 - \mu)$  are always positive,  $x_{rx}(t)$  will always have the same sign as  $x_{rx}(t_{prev})$ . Further generalizing, the value of  $x_{rx}(t)$  after an arbitrary sequence of (eventually

mixed in any order) up and down events is  $x_{rx}(t_{after}) = x_{rx}(t_{before}) \cdot (1 + \mu)^N (1 - \mu)^M$ , where  $N$  and  $M$  are the numbers of up and down events, respectively. As above, given the range of values of  $\mu$ , there is no value of  $N$  and/or  $M$  (and therefore no sequence of events) which can lead to have the sign of the reconstructed signal different from that of the initial value, i.e., to have the reconstructed signal ( $x_{rx}(t)$ ) cross the zero. For this reason, we introduce the zero-crossing event.

---

**Algorithm 1:** Custom event generation scheme
 

---

```

initialize last event as  $E_\uparrow$ 
region_sign = 1
while in acquisition do
  Compute  $\tilde{x}_{TX}[i]$  by resampling
  if  $\tilde{x}_{TX}[i]$  is outside the base region then
    if last event was either  $E_\uparrow$  or  $E_\downarrow$  following  $E_\uparrow$ 
      then
         $\hat{x}_{TX}[i] = region\_sign \times \theta$ 
      else
         $\hat{x}_{TX}[i] \equiv \hat{x}_{\{SoD, Lin, Quad, Avg, PID\}}$ 
      end
    end
    if sign of  $\tilde{x}_{TX}[i] ==$  sign of  $\hat{x}_{TX}[i]$  then
      if  $\mu$  is crossed then
        if sign of  $x_{TX}^\Delta[i] \neq$  sign of  $\tilde{x}_{TX}[i]$  then
          Transmit  $E_\downarrow$ 
        else
          Transmit  $E_\uparrow$ 
        end
      else
        if  $\tilde{x}_{TX}[i-1]$  was inside the base region
          then
            Transmit  $E_\downarrow$ 
          end
        end
      end
    else
      if  $\tilde{x}_{TX}[i-1]$  was inside the base region then
        region_sign = region_sign  $\times$  (-1)
        Transmit  $E_\uparrow$ 
      end
    end
  else
    if  $\tilde{x}_{TX}[i-1]$  was outside the base region then
      Transmit  $E_\uparrow$ 
    end
  end
end
end

```

---

### C. Zero-crossing

The acceleration samples have signed values, as opposed to the capacitance values of a tactile sensor [13] or the grayscale level of a vision sensor [9], [12]. This characteristic, along with the use of a relative threshold, causes a zero-crossing problem to be addressed.

In the communication scheme based on a fixed threshold, the change in the sign of the received value could happen when one out of two possible situations occurs:

- 324 1) an  $E_{\uparrow}$  event is received when  $-\delta(t) < \hat{x}_{RX}(t) < 0$ ;  
 325 2) an  $E_{\downarrow}$  event is received when  $0 \leq \hat{x}_{RX}(t) < \delta(t)$ .

326 By applying the corrections corresponding to the received  
 327 events and described in equation (6), the sign of the received  
 328 signal is changed inherently. As a result, only two types  
 329 of events are required to obtain an unambiguous scheme  
 330 including the generation of events with an absolute threshold.

331 As opposed to that, a relative threshold-based communica-  
 332 tion scheme does not have this capability, because the correc-  
 333 tion is performed by means of a multiplication by a positive  
 334 number. This means that the sign of the estimate cannot  
 335 change, if only  $E_{\uparrow}$  or  $E_{\downarrow}$  polarities are used. In addition, if  
 336 the estimate reaches zero, the following reconstructed values  
 337 are going to be zero for the rest of the acquisition. This will  
 338 be referred to as the “sign change problem” in the following.

#### 339 D. Constraining the relative variation of the input

340 An additional problem introduced by the relative threshold  
 341 is that, when approaching zero, the relative variation of the  
 342 signal is higher and higher. This reduces the effectiveness of  
 343 the resampling strategy employed immediately after the sensor,  
 344 because the signal could double or more from one sample  
 345 to the next (e.g., increasing from 10 mG to 20 mG). Since  
 346 doubling is equivalent to an increase of 100%, the expected  
 347 performance of keeping the relative error under 100 $\mu$ % cannot  
 348 be guaranteed ( $\mu$  is usually set below 1). This will be referred  
 349 to as the “tracking problem” in the following.

#### 350 E. Adopted Solution

351 The tracking problem is solved by the introduction of a base  
 352 threshold ( $\theta$ ), which prevents the system from producing any  
 353 event whenever the absolute value of the input signal is under  
 354 that threshold, as shown in Fig. 2. The value of  $\theta$  depends on:

- 355 • the resolution of the sensor;
- 356 • the relative threshold set for the acquisition;
- 357 • where and how the sensor is physically connected;
- 358 • the external environment.

359 The base threshold could be further tuned after on-field  
 360 simulations.

361 On the other hand, the (relative) data threshold  $\mu$  should be  
 362 a trade-off:

- 363 1) such to obtain a certain maximum relative error out of  
 364 the base region;
- 365 2) low enough to keep a certain compatibility with respect  
 366 to the samples produced by the sensor;
- 367 3) high enough to avoid that the event-rate could increase  
 368 significantly.

369 Once the base region has been introduced, the sign change  
 370 problem is solved by the use of a third type of event called  
 371 “Cross Base”,  $E_{\dagger}$ , which may be produced in two different  
 372 situations:

- 373 1) the last event produced was an  $E_{\uparrow}/E_{\downarrow}$  event;
- 374 2) the last event produced was a  $E_{\dagger}$ .

375 In case 1), the  $E_{\dagger}$  event communicates to the receiver that  
 376 the input signal has just gone under the base threshold, causing  
 377 the estimate to equate  $\pm\theta$ , where the sign is set equal to the

TABLE I: Event coding

Event	Output
$E_{\uparrow}$	10
$E_{\downarrow}$	01
$E_{\dagger}$	11
—	00

378 one of the last predicted value. In case 2), a second  $E_{\dagger}$  after  
 379 another communicates both the exit from the base region and  
 380 the change in the sign of the function. Until the next event,  
 381 the estimate will be  $\mp\theta$ .

382 If, in case 1), after  $E_{\dagger}$  the signal exits the base region with  
 383 the same sign, a  $E_{\downarrow}$  is produced, to allow the algorithm to  
 384 restart computing the estimate with the implemented estima-  
 385 tion algorithm. This solves the sign change problem without  
 386 introducing ambiguities in the communication scheme.

387 Algorithm 1 reports the methodology used to implement the  
 388 complete communication scheme, including the conditions for  
 389 the  $E_{\dagger}$  generation. Because there are three possible events and  
 390 the no event situation, two output lines are used to code the  
 391 events, as reported in Table I.

### 392 III. TAXONOMY OF ASYNCHRONOUS ALGORITHMS

393 Several asynchronous sampling algorithms have been investi-  
 394 gated [1]–[4]. In the application under investigation, the in-  
 395 troduction of the dynamic threshold and the choice of sending  
 396 just events and not the whole sample reduce the quantity of  
 397 the potentially working methods to the magnitude-driven ones  
 398 only. At the beginning, even the integral algorithms have been  
 399 considered. Within this category Send on Area [6] and Send  
 400 on Energy [7] are well-known methods. However, they are  
 401 based on an integral relationship with respect to the original  
 402 signal, so the threshold used concerns the primitive function  
 403 in the Send on Area and the primitive of the signal squared in  
 404 the Send on Energy. This prevents the conceived scheme from  
 405 limiting the maximum relative error on the reconstruction of  
 406 the signal itself, thus this category of algorithms has not been  
 407 considered in the following.

408 On the other hand, the algorithms of the magnitude-driven  
 409 category are characterized by a direct relationship between the  
 410 approximating error and the received signal itself. This feature  
 411 is necessary because all the methods available in the literature  
 412 are based on a static absolute threshold and on the transmission  
 413 of the whole data, whereas the main requirement for the  
 414 system under development is to reduce the output bandwidth.  
 415 Indeed, with the event-based communication scheme defined  
 416 in Section II, only 2 bits per spatial axis would be necessary.

417 Further limitations in the choice of suitable sampling al-  
 418 gorithms depend on the need to limit the complexity of the  
 419 hardware implementation and optimization of resources. After  
 420 taking into account both the mathematical and complexity  
 421 criteria, the following algorithms have been analyzed:

- 422 A. Send on Delta;
- 423 B. Linear;
- 424 C. Quadratic;
- 425 D. Average;

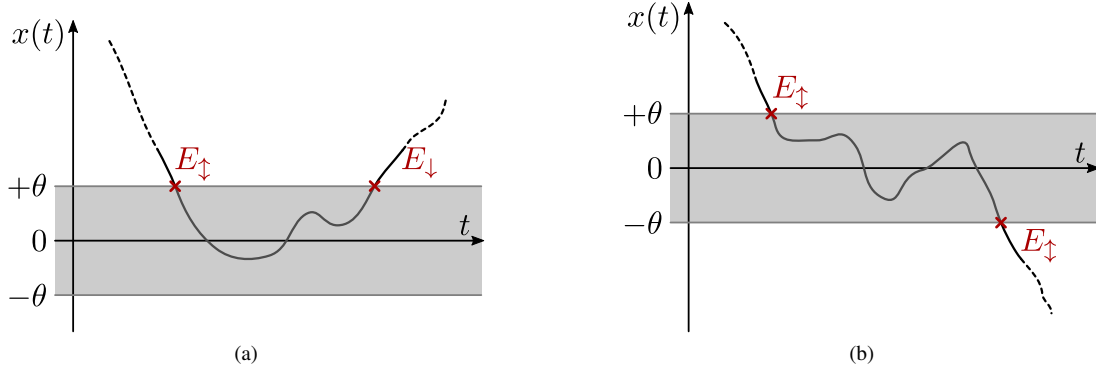


Fig. 2: Zero crossing and base threshold  $\theta$ : when the signal is close to zero, the relative thresholding can cause the generation of way too many events, as the smaller the initial signal is, the finest the sensitivity of the thresholding is. This is solved by setting a “base” threshold. When the signal falls within  $+/-\theta$ , no events are generated. (a,b) clarify the two cases described in the main text, when the signal changes sign.

426 E. Proportional-Integral-Derivative (PID).

427 A. Send on Delta

428 The Send on Delta (SoD) is the most popular algorithm and  
 429 uses the last received value corresponding to the last received  
 430 event, as the estimate for the following samples, until another  
 431 event is received.

432 The approximation  $\hat{x}_{SoD}[i]$  yielded by this algorithm cor-  
 433 responds to a zero-order estimation and the formula is inde-  
 434 pendent of the time elapsed from the last event [1]:

$$\hat{x}_{SoD}[i] \triangleq \hat{x}[i] = \hat{x}[i_L] \quad (11)$$

435 with  $i_L$  the index of the last event.

436 B. Linear

437 The Linear method is based on a first-order approximation  
 438  $\hat{x}_{Lin}[i]$  of the signal [2]:

$$\hat{x}_{Lin}[i] \triangleq \hat{x}[i] = \hat{x}[i_L] + \frac{\hat{x}[i_L] - \hat{x}[i_{L-1}]}{i_L - i_{L-1}} \cdot (i - i_L) \quad (12)$$

439 with  $i_{L-1}$  the index of the last but one event.

440 Differently from the SoD algorithm, the time elapsed from  
 441 the last and last but one events is used to compute the estimate,  
 442 so two events are required to compute the estimate. When no  
 443 event is available or the signal is inside the base region, the  
 444 estimation is based on the Send-On-Delta algorithm with  $\pm\theta$   
 445 as an estimate. When only one event is available (e.g., after  
 446 exiting the base region or after the very first received event),  
 447 the method uses it as  $x^*(t_L)$  and  $\pm\theta$  as  $x^*(t_{L-1})$ .

448 C. Quadratic

449 The Quadratic algorithm, characterized by  $\hat{x}_{Quad}[i]$ , in-  
 450 creases the approximation by one order with respect to the  
 451 Linear method [2]:

$$\begin{aligned} \hat{x}_{Quad}[i] \triangleq \hat{x}[i] = & \hat{x}[i_L] + \frac{\hat{x}[i_L] - \hat{x}[i_{L-1}]}{i_L - i_{L-1}} \cdot (i - i_L) + \\ & + \frac{1}{2} \left[ \frac{\hat{x}[i_L] - \hat{x}[i_{L-1}]}{(i_L - i_{L-1})^2} - \frac{\hat{x}[i_{L-1}] - \hat{x}[i_{L-2}]}{(i_L - i_{L-1}) \cdot (i_{L-1} - i_{L-2})} \right] \cdot \\ & \cdot (i - i_L)^2 \end{aligned} \quad (13)$$

452 Like the Linear algorithm, this method has an intrinsic  
 453 latency, as at least three events out of the base region should  
 454 have been produced to apply the algorithm.

455 In addition, not only does this method require to track the  
 456 time elapsed from the last ( $i_L$ ) and last but one events ( $i_{L-1}$ ),  
 457 it also needs the time elapsed from the last but two event  
 458 ( $i_{L-2}$ ). Until two events are available, it behaves like the  
 459 Linear algorithm; when two events are available,  $\hat{x}[i_{L-2}]$  is  
 460 set to  $\pm\theta$ .

461 D. Average

462 The Average method obtains the estimate  $\hat{x}_{Avg}[i]$  with a  
 463 summation over the last  $M$  predicted values, divided by  $M$ .  
 464 When all the last  $M$  predicted values are equal to each other,  
 465 this method is equivalent to the SoD [3]:

$$\hat{x}_{Avg}[i] \triangleq \hat{x}[i] = \frac{1}{M} \sum_{j=0}^{M-1} \hat{x}[i - j] \quad (14)$$

466  $M$  is chosen depending on the desired number of predicted  
 467 values one would like to consider and the number of available  
 468 memory elements, to store the previous predicted values. In  
 469 the simulations,  $M$  has been set to three, as suggested in [3].  
 470 If less than  $M$  values are available, the average is computed  
 471 on the available number.

472 E. PID

473 The PID algorithm is based on the same theory as in the  
 474 Control Application field. It groups the Send on Delta, Average  
 475 and Linear methods (this last one in a further approximate  
 476 form, to avoid considering the elapsed times), weighing their  
 477 contributions differently [3] into  $\hat{x}_{PID}[i]$ :

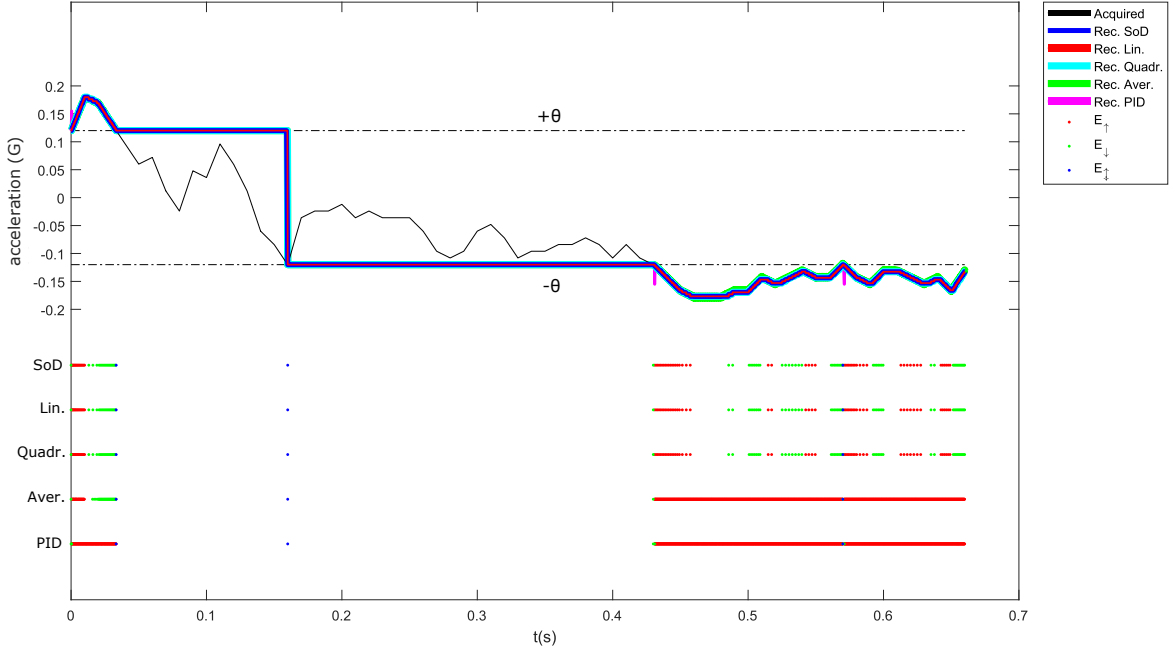


Fig. 3: Event-driven encoding of a signal over time. Top: acquired signal (subset of samples from dataset #8) and reconstructed waveforms using each algorithm, the black lines represent the boundaries of the base region.

Bottom: Events produced by each algorithm with the transmitter fed with the acquired signal. No event is produced during the time interval when the acquired signal is in the base region. At time 0.17 s all the algorithms produce an  $E_{\downarrow}$  when the acquired signal is sampled with opposite sign with respect to the estimate just outside the base region. Consequently, the reconstructed signal changes from  $+\theta$  to  $-\theta$  (falling edge at 0.18 s).

$$\hat{x}_{PID}[i] \triangleq \hat{x}[i] = w_{SoD} \cdot \hat{x}[i_L] + w_{Aver} \cdot \frac{1}{M} \sum_{j=0}^{M-1} \hat{x}[i-j] + w_{Lin} \cdot (\hat{x}[i_L] - \hat{x}[i_{L-1}]) \quad (15)$$

As suggested in [3], the three coefficients have been set to:

- 1)  $w_{SoD} = 0.4$ ;
- 2)  $w_{Aver} = 0.6$ ;
- 3)  $w_{Lin} = 0.3$ .

When less than  $M$  events are available, the estimate is computed for each of the three contributions as previously detailed in the descriptions of the corresponding algorithms.

#### IV. METHODOLOGY

The algorithms have been written in Matlab<sup>®</sup> code and they were simulated with twenty-one heterogeneous datasets as input stimuli (Table II). The first three datasets listed were used because already present in the technical literature [2], [3] and to show that the implemented scheme is general and could be employed on control and medical waveforms as well. The datasets related to the sensor were obtained from real-time acquisitions using a general-purpose computer as data collector from the FPGA, which, in turn, receives data from the accelerometer. Three different situations were used for

TABLE II: Datasets Used for the Algorithm Test.

Dataset #	Content
1	1 <sup>st</sup> order response
2	2 <sup>nd</sup> order response
3	Electro-cardiography
4-6	Sensor manual static XYZ
7-9	Sensor manual tilting XYZ
10-12	Sensor manual shaking XYZ
13-15	Robot motion XYZ
16-18	Robot static XYZ
19-21	Robot shaking XYZ

generating the accelerations: a static one, one tilting the sensor along its Z axis and one shaking the sensor along its X axis. The robotic datasets were acquired on the iCub robot left hand in three different movement conditions, similarly to the sensor data: one static, one moving the arm randomly and one shaking the arm.

The events produced have been collected by a software receiver, which reconstructs the original waveform within a maximum relative error equal to the maximum relative threshold set. The reconstructed waveforms, along with the polarity of the received events for a portion of dataset #8, are shown in Figure 3.



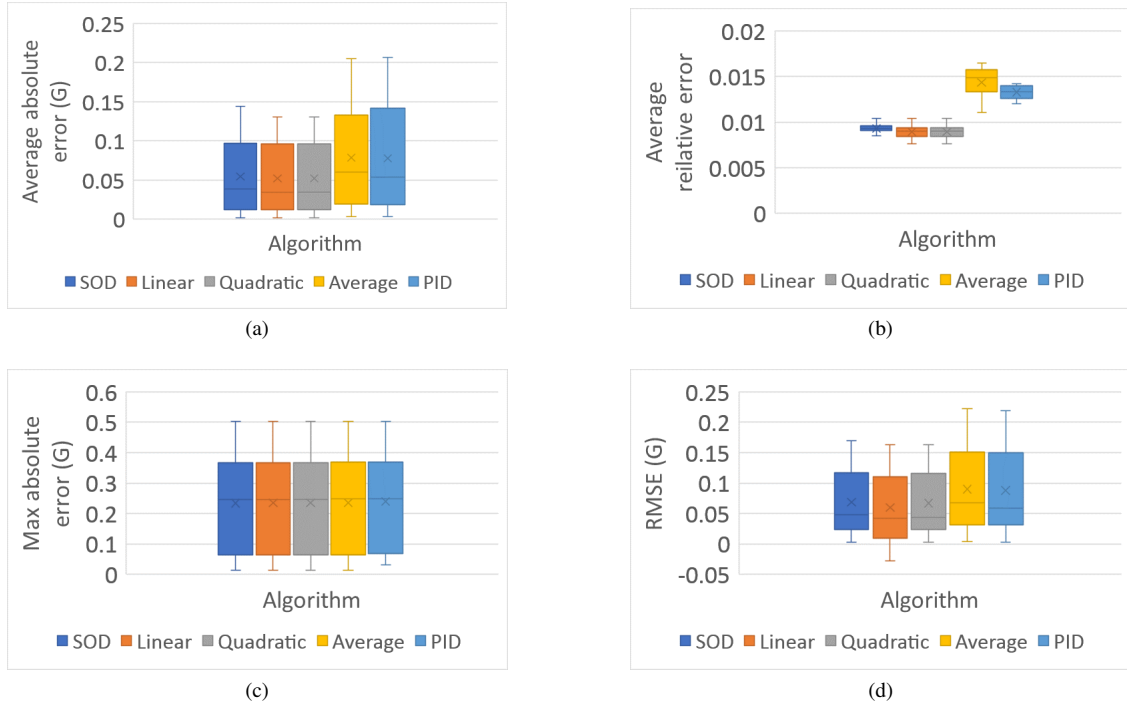


Fig. 4: Results of the simulations: a)  $\gamma_{abs}$ , b)  $\gamma_{rel}$ , c)  $\xi_{abs}$  and d)  $\sigma$ .

508 The performance was evaluated in terms of accuracy, mea-  
 509 sured as error on the reconstructed waveform (i.e., the error  
 510 between the  $\tilde{x}_{RX}(t)$  computed by the RX and the signal  
 511  $\tilde{x}_{TX}(t)$  internally used by the TX to generate the events),  
 512 and effectiveness, measured as the reduction in the number of  
 513 output messages in the conceived event-driven scheme with  
 514 respect to a synchronous transmission. For the sake of clarity  
 515 and without loss of generality, we assume no latency and  
 516 perfect synchronization (same timings) between TX and RX,  
 517 so that we can use the two corresponding discrete-time signals  
 518  $\tilde{x}_{TX}[i]$  and  $\tilde{x}_{RX}[i]$ . In all the simulations,  $\mu$  is set to 0.02, in  
 519 order to have a maximum relative error of 2%. This value has  
 520 been chosen as an acceptable tradeoff between reduced data  
 521 rate and resulting accuracy.

522 Moreover, following the points listed in Section II-C and  
 523 the specifications of the employed accelerometer [23],  $\theta$  is set  
 524 to 0.12 G.

#### 525 A. Accuracy figures

526 The first two performance figures, concerning the accuracy  
 527 evaluation, have an average meaning: the average absolute  
 528 error ( $\gamma_{abs}$ ) and the average relative error ( $\gamma_{rel}$ ) [2].

$$\gamma_{abs} = \frac{1}{N_{samples}} \cdot \sum_{i=n_{in}}^{n_{fin}} |\tilde{x}_{TX}[i] - \tilde{x}_{RX}[i]| \quad (16)$$

$$\gamma_{rel} = \frac{1}{N_{samples}} \cdot \sum_{i=n_{in}}^{n_{fin}} \frac{|\tilde{x}_{TX}[i] - \tilde{x}_{RX}[i]|}{|\tilde{x}_{TX}[i]|} \quad (17)$$

530 where  $n_{in}$  and  $n_{fin}$  are the first sample index and the last  
 531 one, respectively. The average relative error is a factor with

532 respect to the reference. Moreover, the maximum absolute  
 533 ( $\xi_{abs}$ ) and relative ( $\xi_{rel}$ ) errors have been evaluated.

$$\xi_{abs} = \max (|\tilde{x}_{TX}[i] - \tilde{x}_{RX}[i]|) \quad (18)$$

$$\xi_{rel} = \max \left( \frac{|\tilde{x}_{TX}[i] - \tilde{x}_{RX}[i]|}{|\tilde{x}_{TX}[i]|} \right) \quad (19)$$

535 As the signal changes sign, another useful parameter is the  
 536 root mean squared error ( $\sigma$ ):

$$\sigma = \sqrt{\frac{\sum_{i=n_{in}}^{n_{fin}} |\tilde{x}_{TX}[i] - \tilde{x}_{RX}[i]|^2}{N_{samples}}} \quad (20)$$

#### 537 B. Effectiveness figures

538 Two performance figures evaluate the gain of the algorithm,  
 539 where the gain is the number of samples saved by using the  
 540 event-based method instead of a synchronous one.

541 The first figure is the equivalent sampling rate (called  $m$   
 542 in [6]), which is the reciprocal of the average of the inter-  
 543 event intervals:

$$m = \frac{1}{\Delta t_{aver}} = \frac{N_{events}}{\sum_{i=n_{in}}^{n_{fin}} \Delta t_i} \quad (21)$$

544 The second figure is called Effectiveness (also called *energy*  
 545 *ratio* as in [3]):

$$E = \frac{N_{samples}}{N_{events}} \quad (22)$$

546 For example, an Effectiveness equal to  $\sim 10^3$  means that 1  
 547 event every 1000 synchronous samples is sent.

### C. Hardware considerations

The maximum available latency is 50 clock cycles because the input frequency equals 5 MHz from the resampler and the internal working frequency of the target system is 250 MHz (both frequencies are compliant with [20]).

## V. SIMULATION RESULTS

As detailed in the previous paragraphs, the proposed communication system is made of different blocks, each of which has been sized as follows. The resampler unit has 16 fractional bits of precision; the integer part depends on the sensor full scale, which had been set to the maximum available on the specific accelerometer employed in this work, i.e.,  $\pm 16$  G [23]. As a consequence, 6 bits of integer part are required in a signed representation to properly encode even the +16 G value. Moreover, the Linear and Quadratic algorithms also need the inter-event time to be used for the computation, see Eqs. 12) and 13). A 1 s inter-event time could be considered high enough to avoid any timer wrapping, when the acceleration is above the base threshold. In case the acceleration is within the base threshold, a time wrap does not cause any problem because the estimation considers only the base threshold. For a time counter updated at every new sample coming from the resampler, 1 s corresponds to 5 million ticks, i.e., 24 signed bits. For this reason, the integer part of the data is extended to 8 bit and the acceleration data parallelism is set to [8.16] fixed-point representation. As a consequence, the maximum time interval without wrapping is  $2^{23} - 1$ , about 1.68 s.

Figures 4 and 5 show the performance of the different EG algorithms over all the considered datasets. For the accuracy figures ( $\gamma_{abs}$ ,  $\gamma_{rel}$ ,  $\xi_{abs}$  and  $\sigma$ ), the lowest box represents the one which, statistically on the considered datasets, has the best behavior. Conversely, for the effectiveness figures, the situation changes between the equivalent sampling rate ( $m$ ) and the Effectiveness ( $E$ ). The lower the equivalent sampling rate, the better, whereas the lower the Effectiveness the worse. As a preliminary evaluation, the maximum relative error has been verified to be under the desired threshold for all the algorithms.

### A. Accuracy parameters analysis

In terms of Average Absolute Error, the best algorithms are the Linear and Quadratic ones, with the latter being slightly better than the former. Their values extend from 0.01 G to 0.085 G, approximately. The SoD comes immediately afterwards, whereas the Average and PID have a wider dispersion towards higher values, greater than 0.1 G, with the PID being slightly better than the Average.

In terms of Average Relative Error, the best algorithms are, again, the Linear and Quadratic ones, but in this case the former extends more than the latter in the low-value zone of the error, arriving at 0.4 %, with the upper boundary at 0.7 %. The Send on Delta is again the third best algorithm, exhibiting a very narrow dispersion around 0.9 %. The Average remains the worst, followed by the PID, extending over 1.2 %.

For what concerns the Maximum Absolute Error, the distributions are almost the same for all the algorithms, with the 25<sup>th</sup> and 75<sup>th</sup> percentiles between 0.06 G and 0.37 G.

The Root Mean Squared Error shows a situation very similar to the Average Absolute Error case, where the Linear and Quadratic algorithms are very close to each other, with a distribution between 0.02 G and 0.12 G. The Average is still the worst one, followed by the PID and the SoD.

### B. Effectiveness parameters analysis

For the effectiveness figures, the Equivalent Sampling Rate shows a very narrow distribution for the Linear and Quadratic algorithms, meaning that their gain is almost independent of the trend of the input signal. The Linear is slightly better because its box extends partially under the one of the Quadratic. The SoD extends more towards high values, until  $576 \text{ events/s}$ , approximately. The Average remains the worst one even in this case, followed by the PID.

In the end, for the Effectiveness, the first and second order waveforms show that the SoD, Linear and Quadratic have the same performances. However, when considering the remaining 10 datasets a significant difference is shown between the Linear-Quadratic pair and the SoD algorithms: if the former extends between  $2.9 \cdot 10^4 \text{ samples/event}$  and  $7.0 \cdot 10^4 \text{ samples/event}$ , the latter box is comprised between  $2.1 \cdot 10^4 \text{ samples/event}$  and  $4.8 \cdot 10^4 \text{ samples/event}$ . The SoD is below, and the Average and PID methods are even lower than the other ones.

More in detail, the performance of the SoD equals the ones of the Linear and Quadratic methods for the datasets acquired with a manual movement of the accelerometer. On the other hand, the Linear and Quadratic algorithms are always better than the SoD on the robotic datasets, with:

- Accuracy parameters: -0.4 % up to -26.7 % over SoD (-5.4 % avg.);
- Equivalent sampling rate: -7 % up to -58 % over SoD (-20.0 % avg.);
- Effectiveness: +8 % up to +142 % over SoD (+48.0 % avg.).

This analysis allows to conclude that the best methods are the Linear and Quadratic, followed by the SoD. As the other two algorithms are more complex and show worse performance than the SoD, they are not addressed in the following part of this work.

## VI. HARDWARE IMPLEMENTATION

The conceived algorithmic scheme has been described in VHDL to be implemented onto an FPGA platform. In order to achieve the target operating frequency, pipeline stages have been added inside the hardware block. The number of pipeline stages from input to output is however limited from the 50 clock cycles latency requirement. The available FPGA is a speed-grade 1, the lowest speed-grade for the Xilinx Artix-7 XC7A35T model. As a consequence, the number of pipeline stages was tuned until the target frequency was met and the latency requirement was not exceeded (see Section IV-C). This led to a  $\frac{N}{2}$  pipe stages inside the multipliers and  $N$  inside the divider employed in the Linear and Quadratic algorithms, with  $N = 24$  as detailed in Section V. While for the Linear the total latency in the worst case (the one requiring the estimation correction) is within 50 clock cycles, the Quadratic exceeds

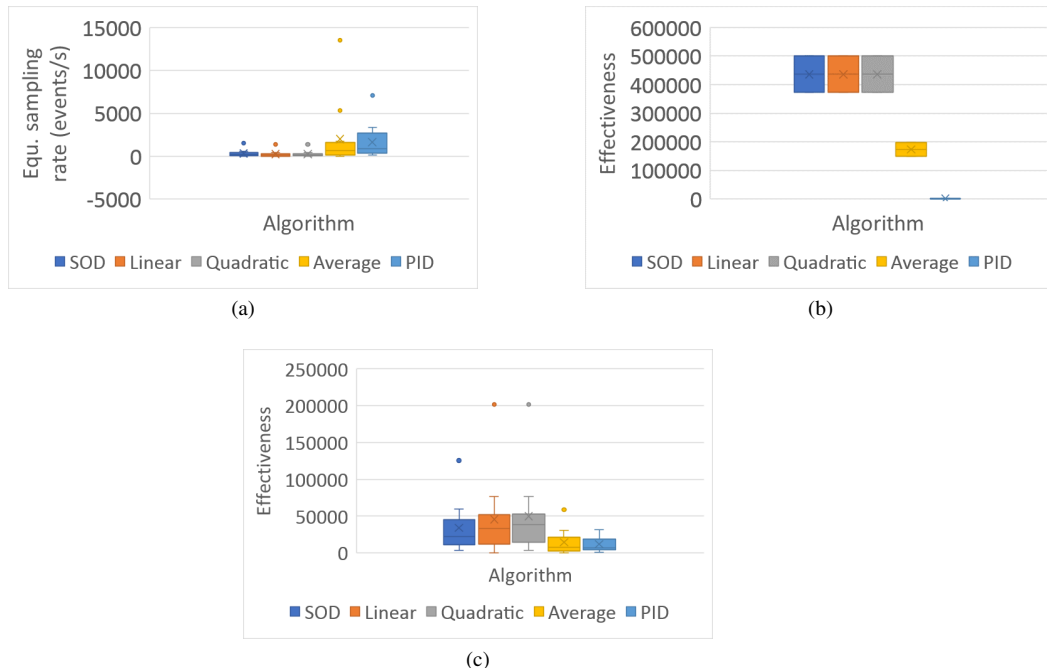


Fig. 5: Results of the Matlab<sup>®</sup> simulations: a) Equivalent Sampling Rate (m), b) Effectiveness related to the first two datasets and c) Effectiveness for all the remainder datasets.

658 this limit. Moreover, the performance parameters show that  
 659 the 2<sup>nd</sup> order term does not give any appreciable advantage  
 660 over the Linear algorithm. These two considerations allow to  
 661 discard the Quadratic algorithm.

662 Finally, considering both the algorithmic performance and  
 663 hardware optimization, the Linear and Send-on-Delta algo-  
 664 rithms appear the most suitable to be mapped onto the FPGA.

665 Since the employed transducer is a tri-axis accelerometer,  
 666 the hardware blocks implementing the resampling and the  
 667 estimation have been replicated once per each axis. The  
 668 complete architecture is shown as a block diagram repre-  
 669 sentation in Figure 6. The SPI Manager block acquires the  
 670 synchronous samples from the accelerometer by using a 4-  
 671 wire SPI communication. Then, it splits the data of each  
 672 axis and feeds them to the corresponding resampling block.  
 673 The output event lines consist, each, in a 6-bit address that  
 674 identifies the axis and the accelerometer, followed by the 2-  
 675 bit event information in the LSBs. Keeping the address inside  
 676 the transmitted data is useful in case the event stream from the  
 677 accelerometer shares the output channel of the system, where  
 678 it is embedded, with other event streams coming from different  
 679 sensors. This allows the receiving end to acknowledge the  
 680 source of the arriving events and is based on the Address-  
 681 Event-Representation (AER) [15]–[17]. Moreover, if the 3  
 682 event lines are multiplexed at the transmitter, only 8 bits  
 683 instead of 24 are present, further reducing the routing cost.

684 Figure 7 shows the hardware arrangement. The MEMS  
 685 accelerometer is connected to an Arty board, hosting an Artix-  
 686 7 FPGA. The connection is achieved by using a series of  
 687 jumpers toward one of the PMOD connectors of the Arty  
 688 board. The board is also connected to a general-purpose  
 689 computer with two cables: the black one in Figure 7 is a

690 USB cable, used to program the FPGA and to receive the  
 691 raw acceleration samples from the FPGA; the white one is an  
 692 Ethernet cable, for collecting the events from the FPGA. The  
 693 Ethernet payload contains the data coded in AER.

#### 694 A. Results

695 Table III shows the post-implementation complexity (esti-  
 696 mated by Xilinx Vivado<sup>®</sup> software) for the single EG block  
 697 when it implements either the SoD or the Linear algorithm.  
 698 By replicating it 3 times and adding the SPI Manager block  
 699 and the resamplers, the LUT usage is 2892 elements (13.9 %  
 700 of the total) and the FF usage is 3620 elements (8.7 % of  
 701 the total) for the Linear case. The block works reliably at the  
 702 target frequency of 250 MHz.

703 In order to evaluate the improvement with respect to a  
 704 synchronous system, the output bandwidth is estimated as:

$$BW_o = o_b \sum (m) \quad (23)$$

705 where  $o_b$  is the number of output bits and  $\sum (m)$  is the sum  
 706 of the equivalent sampling rates obtained on each axis, due to  
 707 the multiplexed output. It is substituted with the fixed output  
 708 data rate of the accelerometer in the synchronous system.

#### 709 B. Hardware setup

710 The synchronous system has a multiplexed output, for a  
 711 symmetrical comparison to the event-driven one. As a result,  
 712 the synchronous system has an 18-bit output data (6-bit  
 713 address and 12-bit acceleration data). The worst-case situation  
 714 for the Manual acquisitions is the shaking case (datasets 10-  
 715 12) with  $\sum (m) = 753.9 \text{ events/s}$ . The worst-case situation for

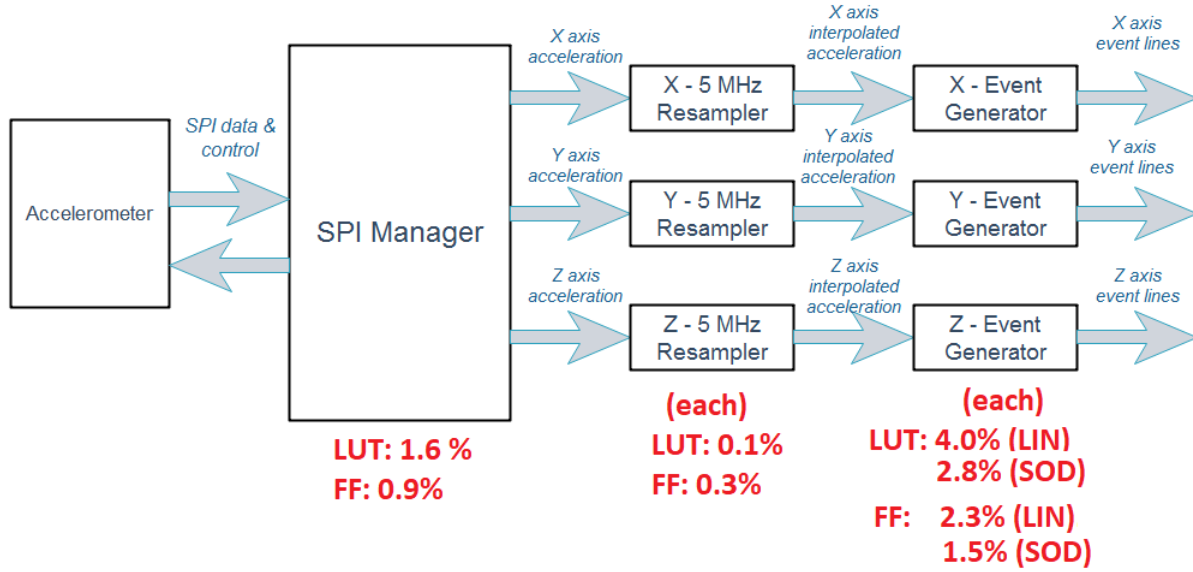


Fig. 6: Block diagram of the complete hardware architecture and relative resource usage of every block after implementation on a Xilinx XC7A35T-L1 FPGA.

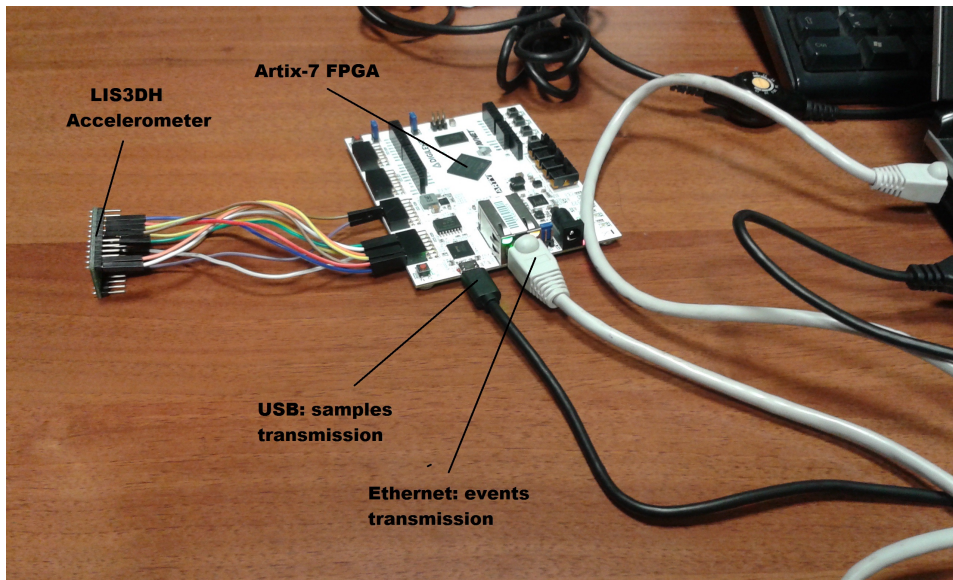


Fig. 7: Hardware setup for the real-time acquisition.

716 the Robotic datasets is the static case (datasets 13-15) with  
 717  $\sum(m) = 1698.0 \text{ events/s}$ . The synchronous data, corresponding  
 718 to the previous two categories of datasets, are produced by the  
 719 accelerometer at 1344 Hz.

720 Figure 8 shows the reconstructed waveforms using SoD and  
 721 Linear algorithms on ten out of the twenty-one considered  
 722 datasets.

723 The performance of the algorithmic block on a single-output  
 724 data are also considered for the first 3 datasets, which are  
 725 generic waveforms. In that case the worst-case equivalent sam-  
 726 pling rate is  $229.5 \text{ events/s}$ , obtained with the Medical waveform  
 727 (dataset #3, Figure 8c). The synchronous data rate for that  
 728 dataset is 360 Hz. The  $BW_o$  variation is shown in Table IV,  
 729 when switching from a synchronous transmission to an event-

TABLE III: Complexity of the implemented algorithms on Xilinx XC7A35T-L1 FPGA.

Block/Port	SoD	Linear
LUTs	582 (2.8 %)	842 (4.0 %)
FF	624 (1.5 %)	969 (2.3 %)
BRAM	0 (0 %)	0 (0 %)
IO	30 (14.3 %)	30 (14.3 %)
BUFG	2 (6.3 %)	2 (6.3 %)
MMCM	1 (20 %)	1 (20 %)

driven one operating on the same input datasets.

As it can be observed, when the movement has a full

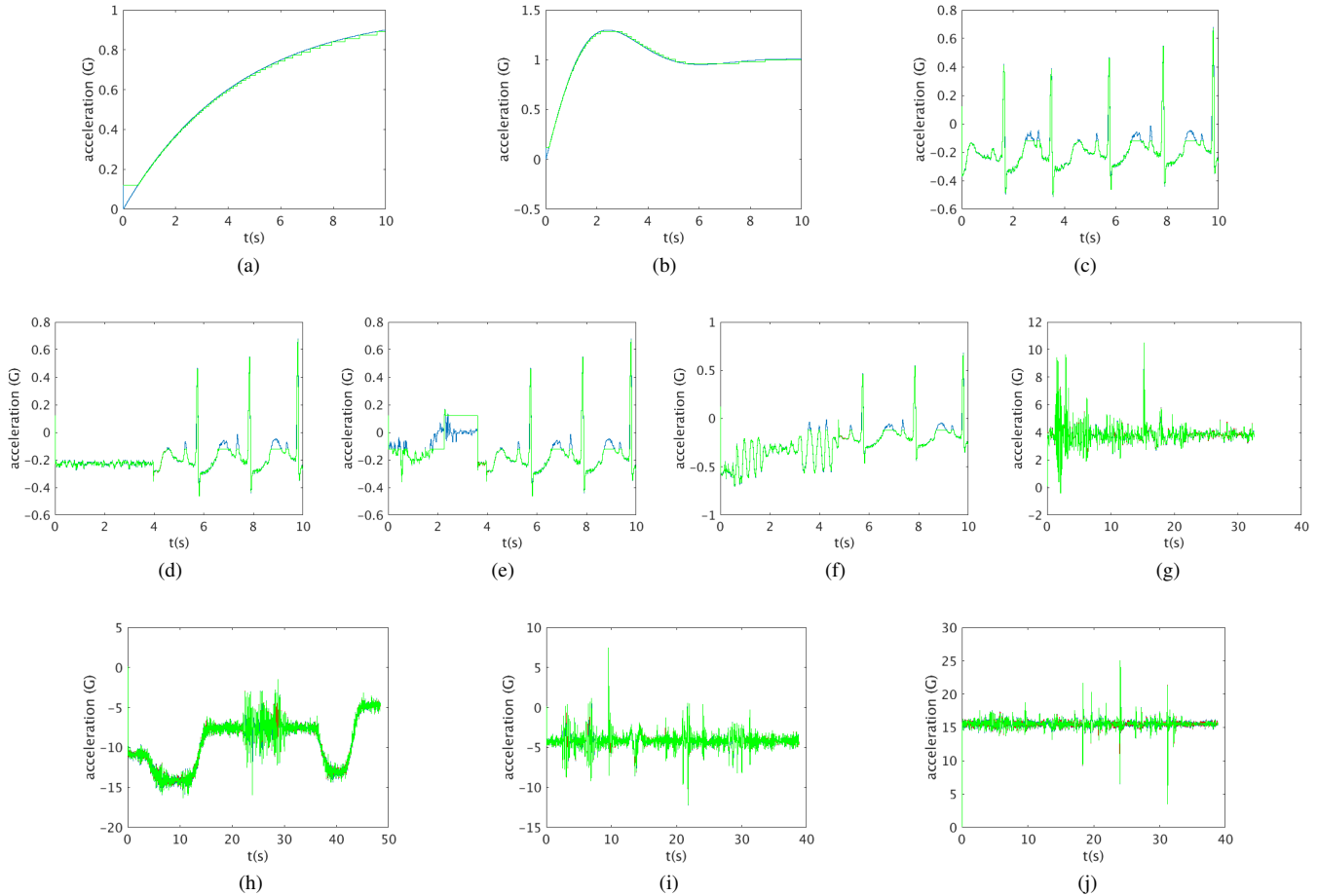


Fig. 8: Example of the considered datasets. the waveforms include the input resampled data (blue), the reconstructed signal with a Linear algorithm (green), the reconstructed signal with a SoD algorithm (red) : a) dataset #1, b) dataset #2, c) dataset #3, d) dataset #4, e) dataset #7, f) dataset #10, g) dataset #14, h) dataset #16, i) dataset #19, j) dataset #21.

TABLE IV: Output Bandwidth Comparison.

Datasets	Synchr. (kbps)	Event-dr.(kbps)	Difference
Manual	24.2	6.0	-75 %
Robotic	24.2	13.6	-44 %
CNTRL & Medical	6.5	1.8	-72 %

732 dynamic within  $\pm 2G$ , i.e., for a manual movement, the  
 733 SoD yields the same performance as the Linear, being very  
 734 attractive for its reduced complexity. In the robotic equipment,  
 735 instead, the Linear algorithm performs better as discussed in  
 736 Section V.

VII. CONCLUSION

738 This paper has detailed the entire process aimed at conceiv-  
 739 ing a new event-driven scheme, identifying the best event-  
 740 generation algorithm from accuracy, effectiveness and imple-  
 741 mentation points of view. Both the communication scheme and  
 742 the algorithm were mapped onto an FPGA hardware to code  
 743 the information received from a digital MEMS accelerometer.  
 744 Experimental results show that the best estimation algorithm

is the first-order, or Linear, one. The real-time acquisitions  
 show that the maximum relative error is kept bounded within  
 the desired relative threshold set at the beginning of the  
 acquisition. The total resource usage in a low-cost FPGA does  
 not exceed the 15 % of both the logic cells and flip-flops. The  
 output bandwidth, thanks to both the 8-bit output event coding  
 and the obtained Effectiveness, is reduced by more than 40 %  
 in all the acceleration datasets, with a -44 % improvement in  
 the robotic platform case. An improvement of -72 % is also  
 observed for single waveforms with slower synchronous data  
 rate.

Although the analysis of the event-driven generation meth-  
 ods has been performed using an accelerometer as input  
 device, the formulation, characterization and FPGA imple-  
 mentation are general enough to hold for different types of  
 sensors, as needed in a fully event-driven robotic sensing  
 system. The main advantages of the event-driven approach  
 are low latency and compression. Our accuracy results show  
 that the compression does not decrease the information content  
 gathered by the sensor. The challenge in the design of artificial  
 perception based on this principle is that of finding principled  
 methods to extract this information without resorting to signal

745  
746  
747  
748  
749  
750  
751  
752  
753  
754  
755  
756  
757  
758  
759  
760  
761  
762  
763  
764  
765  
766



reconstruction and “traditional” algorithms. A fair amount of work has been published so far on the development of such methods, mostly on vision for robots. All the methods and results reported so far show that not only “frame” reconstruction is unnecessary, but also that those algorithms are robust to noise and to the loss of few events (hence having some drop in accuracy). This work goes in the direction of making other sensory modalities available to roboticists to develop multi-modal perception systems that improve efficiency, robustness and autonomy of robots, developing event-driven multi-sensory perception algorithms, ready for when native event-driven sensors will be mature enough to be integrated in robots. In the specific case of accelerometers, the information gathered from the sensor will be useful to assess the movement of the robot, or to detect impact on surfaces, or to classify roughness of surfaces from vibrations. In the first case, the latency of the signal is crucial to detect the contact and correct the action; in the second case, the frequency content of the signal, rather than the acceleration instantaneous value, is important. To study all these aspects, future work includes the integration of the designed system into the iCub robot and the substitution of the Ethernet output with the custom serial protocol discussed in [20], for event transmission in AER packets.

Additionally, the design is fully-portable to other platforms, like ASICs. We will hence develop custom chips with event-driven event generation for off-the-shelf sensors to reduce size and power consumption due to the use of the FPGA. Further developments include the implementation of neural algorithms instead of asynchronous sampling ones and the design of an event-driven readout accelerometer which uses the conceived communication scheme and algorithm internally.

#### AUTHORS’ NOTICE

The material (i.e., the source code and datasets) presented in this work could be provided by the authors upon request.

#### REFERENCES

- [1] M. Miskowicz, “Send-on-delta concept: An event-based data reporting strategy”, in *Sensors*, v. 6, pp. 49-63, 2006.
- [2] K. Staszek, S. Koryciak, M. Miskowicz, “Performance of send-on-delta sampling schemes with prediction”, in *Proceedings of IEEE International Symposium on Industrial Electronics ISIE 2011*, pp. 2037-2042, June 2011.
- [3] F. Xia, Z. Xu, L. Yao, W. Sun, M. Li, “Prediction-based data transmission for energy conservation in wireless body sensors”, in *Proceedings of Wireless Internet Conf. WICON 010*, pp. 1-9, March 2010.
- [4] Various authors, *Event-Based Control and Signal Processing*, ed. By M. Miskowicz, CRC Press, 2016.
- [5] M. Simonov, G. Chicco and G. Zanetto, “Event-Driven Energy Metering: Principles and Applications”, in *EEE Transactions on Industry Applications*, vol. 53, no. 4, pp. 248-251, July-Aug. 2017. doi: 10.1109/TIA.2017.2679680
- [6] M. Miskowicz, “The event-triggered integral criterion for sensor sampling”, in *Proceedings of IEEE International Symposium on Industrial Electronics ISIE 2005*, v. 3, pp. 1061-1066, November 2005.
- [7] M. Miskowicz, “Efficiency of event-based sampling according to error energy criterion”, in *Sensors*, v. 10, n. 3, pp. 2242-2261, 18 Mar. 2010.
- [8] Posch, C., Matolin, D. and Wohlgenannt, R., “A QVGA 143dB Dynamic Range Asynchronous Address-Event PWM Dynamic Image Sensor with Lossless Pixel-Level Video Compression”, in *2010 IEEE International Conference on Solid-State Circuits (ISSCC)*, 7-11 Feb. 2010.

- [9] Posch, C., Matolin, D. and Wohlgenannt, R., “An asynchronous time-based image sensor”, in *2008 IEEE International Symposium on Circuits and Systems (ISCAS)*, pp. 2130-2133, 18-21 May 2008.
- [10] P. Lichtsteiner, C. Posch and T. Delbruck, “A 128×128 120dB 30mW asynchronous vision sensor that responds to relative intensity change”, in *2006 IEEE International Solid State Circuits Conference - Digest of Technical Papers*, San Francisco, CA, 2006, pp. 2060-2069.
- [11] V. Chan, S.-C. Liu and A. van Schaik, “AER EAR: A matched silicon cochlea pair with address event representation interface”, in *IEEE Transactions on Circuits and Systems I*, 2007, pp. 48-59, vol. 54(1).
- [12] B. Son, Y. Suh, S. Kim, H. Jung, J. Kim, C. Shin, K. Park, K. Lee, J. Park, J. Woo, Y. Roh, H. Lee, Y. Wang, I. Ovsianikov and H. Ryu, “4.1 A 640×480 dynamic vision sensor with a 9um pixel and 300Meps address-event representation”, in *2017 IEEE International Solid-State Circuits Conference (ISSCC)*, San Francisco, CA, 2017, pp. 66-67.
- [13] E. Baglini, G. Cannata and F. Mastrogiovanni, “Design of an embedded networking infrastructure for whole-body tactile sensing in humanoid robots” in *10th IEEE-RAS International Conference on Humanoid Robots*, 2010.
- [14] L. Osborn, R. R. Kaliki, A. B. Soares and N. V. Thakor, “Neuromimetic event-based detection for closed-loop tactile feedback control of upper limb prostheses”, in *IEEE Transactions on Haptics*, vol. 9, no. 2, pp. 196-206, April 2016.
- [15] M. Sivilotti “Wiring Considerations in analog VLSI Systems with Application to Field-Programmable Networks”, 1991.
- [16] A. Linares-Barranco, G. Jimenez-Moreno, A. Civit-Ballcells and B. Linares-Barranco, “On synthetic AER generation”, in *2004 IEEE International Symposium on Circuits and Systems (IEEE Cat. No.04CH37512)*, 2004, pp. V-784-V-787 Vol.5.
- [17] R. Paz-Vicente, A. Linares-Barranco, A. Jimenez-Fernandez, G. Jimenez-Moreno and A. Civit-Balcells, “Synthetic retina for AER systems development”, in *2009 IEEE/ACS International Conference on Computer Systems and Applications*, Rabat, 2009, pp. 907-912.
- [18] P. Motto Ros, M. Crepaldi, C. Bartolozzi and D. Demarchi, “A hybrid quasi-digital/neuromorphic architecture for tactile sensing in humanoid robots”, in *Advances in Sensors and Interfaces (IWASI), 2015 6th IEEE International Workshop on Advances in Sensors and Interfaces*, June 2015.
- [19] P. Motto Ros, M. Crepaldi, C. Bartolozzi and D. Demarchi, “Asynchronous DC-free serial protocol for event-based AER systems”, in *2015 IEEE International Conference on Electronics, Circuits, and Systems (ICECS)*, Cairo, 2015, pp. 248-251. doi: 10.1109/ICECS.2015.7440295
- [20] C. Bartolozzi, P. Motto Ros, F. Diotalevi, N. Jamali, L. Natale, M. Crepaldi and D. Demarchi, “Event-driven encoding of off-the-shelf tactile sensors for compression and latency optimisation for robotic skin”, in *2017 IEEE/RSJ International Conference on Intelligent Robots and Systems (IROS)*, Vancouver, BC, 2017, pp. 166-173.
- [21] S. Caviglia, L. Pinna, M. Valle, and C. Bartolozzi, “An event-driven POSFET taxel for sustained and transient sensing”, in *2016 IEEE International Symposium on Circuits and Systems (ISCAS)*, pp. 349-352, May 2016.
- [22] F. Bergner, E. Dean-Leon, and G. Cheng, “Event-based signaling for large-scale artificial robotic skin — realization and performance evaluation”, in *2016 IEEE/RSJ International Conference on Intelligent Robots and Systems (IROS 2016)*, October 2016.
- [23] ST Microelectronics, *LIS3DH - MEMS digital output motion sensor: ultra-low-power high-performance 3-axis “nano” accelerometer*, December 2016.
- [24] A. Parmiggiani, M. Maggiali, L. Natale, F. Nori, A. Schmitz, N. Tsagarakis, J. Victor, F. Becchi, G. Sandini, G. Metta, “The design of the iCub humanoid robot”, in *International Journal of Humanoid Robotics*, vol. 09, no. 04, 1250027, 2012.

888 **Marino Laterza** is Fellow researcher at Istituto Italiano di Tecnologia.  
889 He received the Bachelor's Degree in Electronic Engineering (Summa cum  
890 Laude) in 2015 and the Master of Science in Electronic Engineering in 2017  
891 (Summa cum Laude), both from Politecnico di Torino, Italy. His interests  
892 regard digital hardware design on both programmable and application-specific  
893 platforms. His current research is focused on the implementation of neural  
894 models on FPGA to emulate human perception in tactile sensing.

895 **Paolo Motto Ros** Paolo Motto Ros is Senior Post-Doc researcher at Istituto  
896 Italiano di Tecnologia, Electronic Design Laboratory. He received the elec-  
897 tronic engineering degree and the Ph.D. in electronic engineering from the  
898 Politecnico di Torino (Polito), Turin, Italy, in 2005 and 2009, respectively.  
899 From 2009 to 2012 he was with Neuronica Laboratory (Dipartimento di Elet-  
900 tronica, Politecnico di Torino) as Post-Doc, working on assistive technologies,  
901 computer vision and learning machines projects. He joined the Center for  
902 Space Human Robotics (CSHR), Istituto Italiano di Tecnologia (IIT), Turin,  
903 Italy, in 2012; since 2016 he is with Electronic Design Laboratory (EDL),  
904 IIT, Genoa, Italy. He is an IEEE member since 2016, and member of the  
905 Circuits And Systems (CAS) society. He counts >20 publications; current  
906 research include design of full-custom ultra-low-power asynchronous digital  
907 integrated circuits, event-based smart-sensors, sensor networks, bio-inspired  
908 electronics, neuromorphic engineering.

909 **Danilo Demarchi** Associate Professor at Politecnico di Torino, Italy, De-  
910 partment of Electronics and Telecommunications. Lecturer at EPFL Lau-  
911 sanne, Switzerland, Adjunct Professor at Tongji University Shanghai, China,  
912 Associate Faculty at the University of Illinois at Chicago, Department of  
913 Electrical and Computer Engineering. Leading the MiNES (Micro&Nano  
914 Electronic Systems) Laboratory of Politecnico di Torino. Senior Member of  
915 IEEE, Member of the BioCAS Technical Committee, Associate Editor of  
916 the Transactions on Biomedical Circuits and Systems (TBioCAS), Associate  
917 Editor of IEEE Sensors and of the Springer Journal BioNanoScience. General  
918 Chair of BioCAS 2017 (Biomedical Circuits and Systems) Conference edition  
919 in Torino.

920 **Maurizio Martina** Maurizio Martina (IEEE Senior Member) is associate  
921 professor at Politecnico di Torino. He received the electronic engineering  
922 degree and the Ph.D. in electronic engineering from the Politecnico di  
923 Torino in 2000 and 2004, respectively. From 2004 he is with the VLSI-  
924 lab (Electronics and Telecommunications Department, Politecnico di Torino)  
925 working on VLSI architectures for digital signal processing. He is author and  
926 coauthor of about 100 scientific papers.

927 **Chiara Bartolozzi** Chiara Bartolozzi (IEEE Member) is researcher at the  
928 Istituto Italiano di Tecnologia. She earned a degree in Engineering (with  
929 honors) at University of Genova (Italy) and a Ph.D. in Neuroinformatics  
930 at ETH Zurich, developing analog subthreshold circuits for emulating bio-  
931 physical neuronal properties onto silicon and modelling selective attention on  
932 hierarchical multi-chip systems. She is currently leading the Event Driven  
933 Perception for Robotics group ([www.edpr.iit.it](http://www.edpr.iit.it)), mainly working on the appli-  
934 cation of the "neuromorphic" engineering approach to the design of sensors  
935 and algorithms for robotic perception. She is chair of the Neuromorphic  
936 Systems and Application Technical Committee of IEEE CAS.